Arch. Mech., **67**, 1, pp. 3–24, Warszawa 2015

Theoretical study on thermal and structural phenomena in thin elements heated by a laser beam

M. KUBIAK[1)], W. PIEKARSKA[1)], R. PARKITNY[2)]

[1)] *Institute of Mechanics and Machine Design Foundations*
Częstochowa University of Technology
Dąbrowskiego 73, 42-200 Częstochowa, Poland
e-mails: kubiak@imipkm.pcz.pl,
piekarska@imipkm.pcz.pl

[2)] *Katowice School of Technology*
Rolna 43, 40-555 Katowice, Poland
e-mail: parkitny@gmail.com

This paper concerns the mathematical and numerical modelling of thermal phenomena and phase transformations in the solid state accompanying laser heating processes. Thermal phenomena with the motion of a liquid metal in the fusion zone are analyzed on the basis of numerical solution of equations for mass, momentum and energy conservation. Phase transformations in solid state are estimated using classic models of the kinetics of phase transformations as well as continuous heating transformations (CHT) and continuous cooling transformations (CCT) diagrams for S355 steel. Computer simulations are executed for the laser welding process in order to predict the influence of welding speed on the structural composition as well as thermal and structural strains in the joint.

Key words: laser processing, heat transfer, fluid flow, phase transformations, numerical modelling.

1. Introduction

Laser technology is implemented in many industries and increasingly used in cutting, surface treatment and welding. Because of technological advantages, the laser successfully displaces conventional production techniques in many applications [1–3]. However, many new phenomena occur in the laser processing of steel that are not found in the conventional treatment of steel. In the case of laser welding a "keyhole" is created with ionised vapour that absorbs the laser beam power. The beam is afterwards transferred to the walls of the "keyhole" forming the fusion zone [4–6]. Moreover, hardening structures occur in the thermal influence zone due to the impact heating and rapid cooling of a material in the process, even in susceptible to the laser processing unalloyed and low-alloy constructional steels. Laser mode, beam radius, laser power and welding speed are the basic factors influencing the geometry of the fusion zone and mechanical properties of the material. Therefore, the knowledge about thermal phenomena and structural transformations is crucial in the prediction of the quality and durability of the construction in terms of different laser beam parameters [7–10].

Theoretical analysis of coupled physical phenomena accompanying laser-material interaction is very complex in terms of mathematical modelling and numerical solutions. Numerical models usually describe chosen phenomena, due to the computational complexity of the problem [7, 8]. Over the last several years, a number of papers concerning the laser heating modelling were presented with different phenomena taken into account, including: thermal, mechanical, electrical and metallurgical phenomena. The temperature field is mainly considered in many studies, without [11–13] or with [9, 14, 15] structural transformations taken into account. However, in the case of material melting by an external heat source, the motion of the liquid material in the melted zone significantly affects the quality of results of computer simulations [5, 7, 16]. Consideration of liquid material motion in the model allows for the analysis of previously neglected phenomena in material melting processes and has a significant impact on the estimated temperature distribution and consequently numerically estimated shape and size of melted zone. Nevertheless, there is still a lack of comprehensive models in the literature allowing the analysis of coupled thermal and structural phenomena when taking into account the motion of liquid material in the fusion zone. In addition, the numerical modelling of thermal and structural deformations is the starting point for the analysis of thermomechanical states in laser heated constructions [8, 17].

This work concerns mathematical and numerical modelling of thermal and structural phenomena occurring in a single laser beam welding of thin elements made of S355 steel. The motion of liquid steel in the fusion zone is taken into

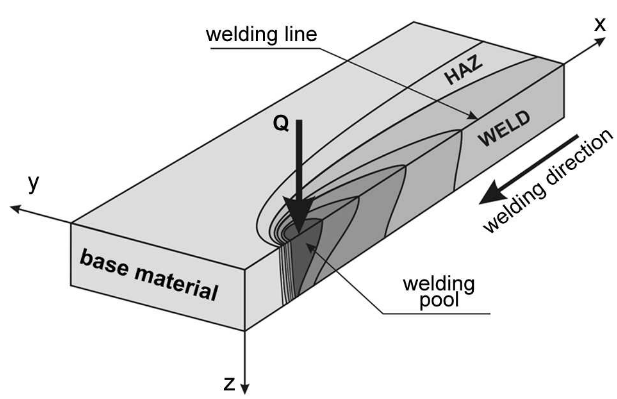

Fig. 1. Scheme of considered process.

considerations in the analysis as well as the latent heat generated during material state changes and the latent heat of phase transformations in the solid state. Temperature field, liquid material velocity field, structural composition and isotropic strain are estimated. Computer simulations are performed for heat source travelling at different speeds. Scheme of considered system is presented in Fig. 1.

2. Thermal phenomena

Temperature field mostly depends on the intensity of heat energy and its distribution in the material. The motion of melted material in the fusion zone is mainly generated by natural convection according to Boussinesq model [5, 7]. Mathematical model assumes fuzzy solidification front between solidus and liquidus temperatures where liquid material motion is treated as a fluid flow through porous medium with respect to Darcy's model [5]. In theoretical considerations latent heat of fusion, evaporation and the latent heat of phase transformations in the solid state are taken into account.

2.1. Governing equations

The temperature field and liquid material velocity field are determined on the basis of the solution of mass, momentum and energy conservation equations, described as follows:

$$\frac{\partial \rho}{\partial t} + \frac{\partial}{\partial x_\alpha}(\rho \mathbf{v}) = 0, \tag{2.1}$$

$$\begin{aligned}
&\frac{\partial(\rho u)}{\partial t} + \frac{\partial}{\partial x_\alpha}(\rho u \mathbf{v}) = -\frac{\partial p}{\partial x} + \frac{\partial}{\partial x_\alpha}\left(\mu \frac{\partial u}{\partial x_\alpha}\right) - \frac{\mu u}{\rho K},\\
&\frac{\partial(\rho v)}{\partial t} + \frac{\partial}{\partial x_\alpha}(\rho v \mathbf{v}) = -\frac{\partial p}{\partial y} + \frac{\partial}{\partial x_\alpha}\left(\mu \frac{\partial v}{\partial x_\alpha}\right) - \frac{\mu v}{\rho K},\\
&\frac{\partial(\rho w)}{\partial t} + \frac{\partial}{\partial x_\alpha}(\rho w \mathbf{v}) = -\frac{\partial p}{\partial z} + \frac{\partial}{\partial x_\alpha}\left(\mu \frac{\partial w}{\partial x_\alpha}\right) + g\beta_T(T - T_s) - \frac{\mu w}{\rho K},
\end{aligned} \tag{2.2}$$

$$C\frac{\partial T}{\partial t} = \frac{\partial}{\partial x_\alpha}\left(\lambda \frac{\partial T}{\partial x_\alpha}\right) - C\frac{\partial T}{\partial x_\alpha}\mathbf{v} + \tilde{Q}, \tag{2.3}$$

where ρ is density [kg/m^3], g is a gravity acceleration, β_T is a thermal expansion coefficient [1/K], μ is a dynamic viscosity [kg/ms], T_s is the solidus temperature, K is the porous medium permeability, $\lambda = \lambda(T)$ is a conductive coefficient [W/mK], $C = C(T)$ is an effective heat capacity, $\tilde{Q}$ is a laser beam heat source power over the area [W/m^3], $\mathbf{v} = v(x_\alpha, t) = (u, v, w)$ is a velocity vector, $T = T(x_\alpha, t)$ is a temperature and x_α is material point coordinate.

Governing equations are completed by the initial and boundary condition. Equation (2.2) is completed by the initial condition $t = 0 : \mathbf{v} = 0$ and the Dirichlet type boundary condition $\mathbf{v}|_{T=T_S} = 0$ at the boundaries of melted zone (determined by the solidus temperature). At the upper surface of the plate the Marangoni effect is considered [11] according to the following formula:

$$\boldsymbol{\tau}_s = \mu \frac{\partial \mathbf{v}}{\partial n} = \frac{\partial \gamma}{\partial T} \frac{\partial T}{\partial s}, \tag{2.4}$$

where τ_s is the Marangoni shear stress in the direction tangent to the surface, γ is surface tension coefficient.

Assuming that mushy zone is composed of a regular matrix of spherical grains submerged in liquid material, the porous medium permeability is given by the Carman–Kozeny equation:

$$K = K_0 \frac{f_L^3}{(1 - f_L)^2}; \qquad K_0 = \frac{d_0^2}{180}, \tag{2.5}$$

where f_L is a porosity coefficient (liquid fraction), d_0 is an average solid particle diameter [m], K_0 is the base porous medium permeability [m^2].

Energy conservation equation (2.3) is completed by the initial condition $t = 0 : T = T_0$ and boundary conditions of Neumann and Newton type taking into account the heat loss due to convection and radiation by

$$\mathit{\Gamma} : -\lambda \frac{\partial T}{\partial n} = \alpha_k (T|_{\mathit{\Gamma}} - T_0) + \varepsilon \sigma (T^4|_{\mathit{\Gamma}} - T_0^4) - q_o + q_v, \tag{2.6}$$

where α_k is a convective coefficient, ε is a radiation coefficient, and σ is the Stefan–Boltzmann constant. Element q_o is the heat flux towards the top surface of the welded element ($z = 0$) in the source activity zone, while q_v represents heat loss due to material evaporation in area where $T \geq T_L$, $\mathit{\Gamma}$ is a boundary of analyzed domain.

The latent heat associated with material state changes is considered in Eq. (2.3). Between solidus and liquidus temperatures $T \in [T_S; T_L]$ (solid-liquid transformation) the latent heat of fusion is taken into account, assuming linear increase of a solid fraction in the mushy zone:

$$C(T) = \rho_{SL} c_{SL} + \rho_S \frac{H_L}{T_L - T_S} \qquad \text{for } T \in [T_S; T_L], \tag{2.7}$$

where H_L [J/kg] is the latent heat of fusion and the product of density and specific heat in the mushy zone equals: $c_{SL}\rho_{SL} = c_S\rho_S(1 - f_L) + c_L\rho_L(f_L)$.

The latent heat of evaporation is considered in temperatures exceeding the boiling point of steel (T_b) [13, 18]. The effective heat capacity for $T \geq T_b$ is expressed as follows:

$$C(T) = \rho_L c_L + \frac{\rho_L H_b}{T_{\max} - T_b} \qquad \text{for } T \geq T_b, \tag{2.8}$$

where H_b [J/kg] is latent heat of evaporation, $T_{\max}$ is a maximum temperature, assumed as 3500 K.

This evaporation model is correct assuming a full equilibrium of metal vapour pressure in the keyhole and a pressure of shielding gases.

Phase transformations in the solid state appear in the cooling process. Heats generated during transformation of austenite into ferrite, pearlite, bainite and martensite are included into the effective heat capacity.

$$C(T) = \begin{cases} \rho_S c_S + \sum\limits_i \rho_S H_i^{\eta_i} \dfrac{d\eta_i(T)}{dT} & \text{for } T \in [T_s^i; T_f^i], \\ \rho_S c_S & \text{for } T \notin (T_s^i; T_f^i), \end{cases} \tag{2.9}$$

where T_s^i and T_f^i are start and final temperatures of each phase transformation, $H_i^{\eta_i}$ is a latent heat of i-th phase transformation, η_i is a volumetric fraction of i-th structural constituent.

Latent heat of austenite transformation into ferrite ($H_{A\to F}$), pearlite ($H_{A\to P}$), bainite ($H_{A\to B}$) and martensite ($H_{A\to M}$) as well as heat capacity of structural constituents of steel are determined by experimental research [14, 19] for appropriate temperatures of transformations, whereas volumetric fraction η_i results from the kinetics of phase transformation.

2.2. Heat sources

A very important issue in the modelling of welding processes is an appropriate selection of the heat source power distribution, primarily responsible for the melted pool shape and the temperature distribution in the material [12, 15, 20–22]. Models of the laser beam heat source power distribution are based on the surface Gaussian distribution, expressed in the general form:

$$Q(r) = \frac{f Q_L}{\pi r_0^2} \exp\left(-f \frac{r^2}{r_0^2}\right), \tag{2.10}$$

where Q_L is a laser beam power [W], r_0 is a beam radius [m], $r = \sqrt{x^2 + y^2}$ is a current radius [m] and coefficient f (usually assumed as $f = 2$) characterizes a beam distribution.

Considerably less study has been devoted to the modelling of the heat source power distribution in terms of deep material penetration. Energy absorption in the laser welding and the immediate transport of the heat below the surface of the workpiece is determined by two mechanisms of Fresnel's absorption and inverse Bremsstrahlung's absorption [4, 6]. The laser beam power distribution is considered as Gaussian-like simplified volumetric heat source in the engineering practice due to the complexity of phenomena. A major problem in developing of simplified models is the determination of the size and shape of the heat source along the thickness of the workpiece that corresponds to the experimental data with appropriate accuracy. From the analysis of the process it is observed that the beam absorption decreases with increasing material penetration. A good approximation of volumetric heat source power distribution is given in universal cylindrical-involution-normal (CIN) [12] heat source model. This model allows for the description of variety volumetric heat source shapes taking into account the relation between heat source power density and material penetration depth (Fig. 2)

$$Q(r,z) = \frac{kK_z\eta_L Q_L}{\pi(1-e^{(K_z s)})} e^{-(kr^2+K_z z)}(1-u(z-s)), \tag{2.11}$$

where Q_L is the laser beam power, η_L is a laser efficiency, $K_z = 3/s$ is a heat source power exponent, $k = 3/r_0^2$ is a beam focus coefficient and s is the heat source beam penetration depth, $u(z-s)$ is a Heaviside function.

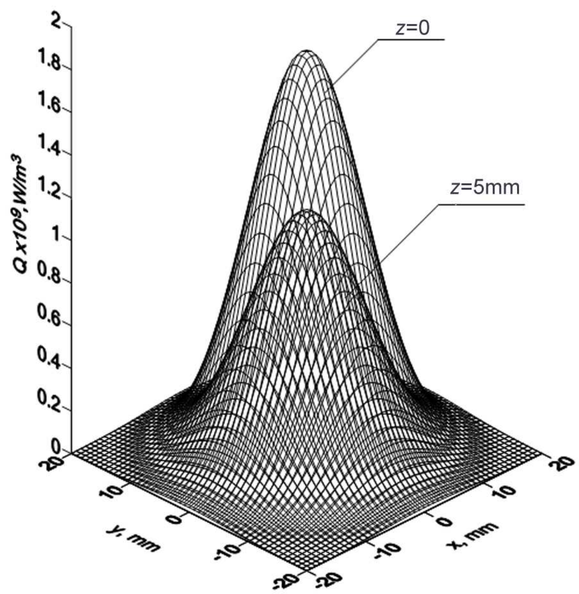

Fig. 2. Exemplary CIN heat source power distribution.

3. Phase transformations in solid state. Thermal and structural strain

Phase transformations in solid state are analyzed during heating and cooling of thin sheets made of S355 steel with chemical composition: 0.19 C, 1.05 Mn, 0.2 Si, 0.08 Cr, 0.11 Ni, 0.006 Al, 0.028 P, 0.02 S [%]. Structure composition is predicted on the basis of classic kinetics of phase transformations models as well as continuous heating transformation (CHT) and continuous cooling transformation (CCT) diagrams with final fractions of structure constituents determined experimentally by dilatometric research [17].

In dilatometric analysis a constant austenitization temperature $T_A = 1100°\mathrm{C}$ was assumed and different heating and cooling rates simulating thermal cycles in laser heating. The microstructure of analyzed samples was afterwards evaluated by microstructure analysis, supported by measurements of microhardness. Obtained diagrams were further discretized using interpolation function of different types. CHT and CCT diagrams are presented in Fig. 3. Corresponding interpolating functions and coefficients are presented in Tables 1-2.

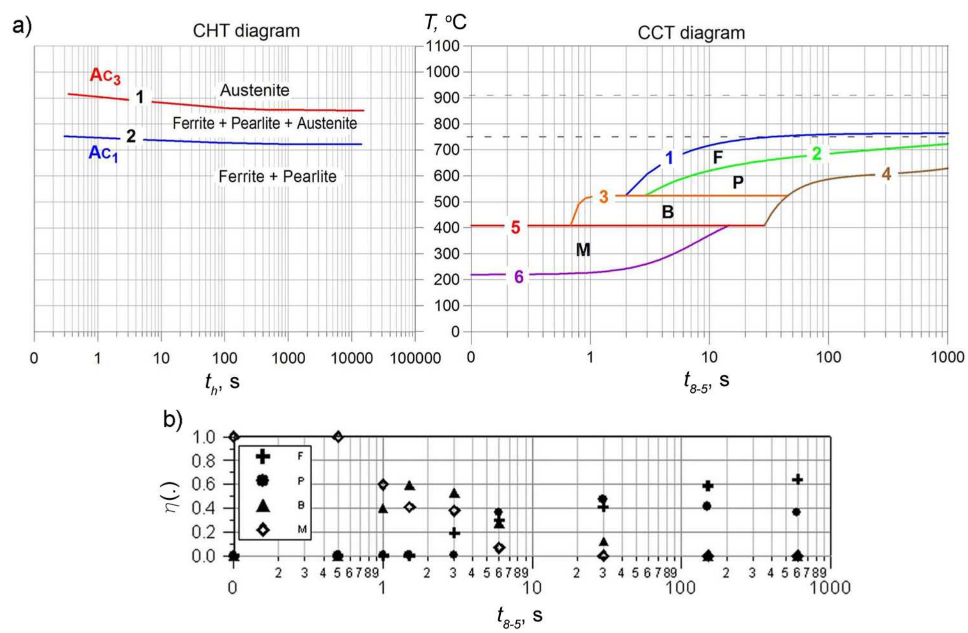

Fig. 3. Interpolated: a) CHT and CCT diagrams, b) final fractions of structure constituents for S355 steel.

The increase of a volumetric fraction of austenite between austenitization temperatures $T \in [\mathrm{Ac}_1; \mathrm{Ac}_3]$ is determined by the Johnson–Mehl–Avrami (JMA) formula taking into account the influence of heating rates on $\mathrm{Ac}_1(t)$ and $\mathrm{Ac}_3(t)$

Table 1. Interpolated CHT diagram.

Curve	Time t_h	Equation	Coefficients
1 - A$_{c1}$	0.30–10 000	$y = \dfrac{A \cdot B + C \cdot t_h^D}{B + t_h^D}$	$A = 757.96$ $B = 2.66$ $C = 720.87$ $D = 0.57$
2 - A$_{c3}$	0.30–10 000	$y = \dfrac{A \cdot B + C \cdot t_h^D}{B + t_h^D}$	$A = 926.36$ $B = 2.63$ $C = 850.90$ $D = 0.60$

Table 2. Interpolated CCT diagram.

Curve	Time t_h	Equation	Coefficients
1 - F$_s$	1.98–1000	$y = A_{Fs} + \dfrac{B_{Fs}}{t_{8-5}}$	$A_{Fs} = 764.38$ $B_{Fs} = -473.38$
2 - P$_s$	2.90–1000	$y = A_{Ps} \cdot B_{Ps}^{1/t_{8-5}} \cdot t_{8-5}^{C_{Ps}}$	$A_{Ps} = 625.49$ $B_{Ps} = 0.56$ $C_{Ps} = 0.02$
3 - B$_s$	0.69–46	$y = \dfrac{A_{Bs} \cdot B_{Bs} + C_{Bs} \cdot t_{8-5}^{D_{Bs}}}{B_{Bs} + t_{8-5}^{D_{Bs}}}$	$A_{Bs} = -745.97$ $B_{Bs} = 0.0034$ $C_{Bs} = 523.30$ $D_{Bs} = 8.92$
4 - P$_f$ +B$_f$	29.10–1000	$y = A_{Pf+Bf} + B_{Pf+Bf} \cdot t_{8-5} + \dfrac{C_{Pf+Bf}}{t_{8-5}^2}$	$A_{Pf+Bf} = 600.22$ $B_{Pf+Bf} = 0.03$ $C_{Pf+Bf} = -161246.52$
5 - M$_s$	0.10–29.10	$y = A_{Ms} + B_{Ms} \cdot t_{8-5}$	$A_{Ms} = 409$ $B_{Ms} = 0$
6 - M$_f$	0.10–14.50	$y = \dfrac{A_{Ms} \cdot B_{Ms} + C_{Ms} \cdot t_{8-5}^{D_{Ms}}}{B_{Ms} + t_{8-5}^{D_{Ms}}}$	$A_{Mf} = 219.43$ $B_{Mf} = 32.36$ $C_{Mf} = 484.25$ $D_{Mf} = 1.64$

temperatures (Fig. 3a)

$$\tilde{\eta}_A(T,t) = \eta_{(\cdot)}(1 - \exp(-b\, t^n), \tag{3.1}$$

where $\eta_{(\cdot)}$ is a sum of volumetric fractions of base material structure ($\eta_{(\cdot)} = 1$), coefficients $b = b(T)$ and $n = n(T)$ are determined by starting ($\eta_s = 0.01$) and final ($\eta_f = 0.99$) conditions for phase transformation as follows:

$$b(T) = -\frac{\ln(\eta_f)}{(t_s)^{n(T)}}, \qquad n(T) = \frac{\ln(\ln(\eta_f)/\ln(\eta_s))}{\ln(t_s/t_f)}, \tag{3.2}$$

where t is a time, $t_s = t_s(T_{sA})$ and $t_f = t_f(T_{fA})$ are phase transformation start and final times, T_{sA} i T_{fA} are start and final temperatures ($Ac_1(t)$ and $Ac_3(t)$ for heating process).

In the case of incomplete austenitization [17, 23] (where maximum temperature of thermal cycle $T_{\max}$ is found between $[A_{c1} \div A_{c3}]$), a fraction of austenite formed during heating is determined according to the following relation:

$$\eta_A = (T_{\max} - Ac_1(t))/(Ac_3(t) - Ac_1(t)). \tag{3.3}$$

The base material structure (untransformed into the austenite) is defined as a sum of fractions $\eta_k = (1 - \eta_A)$. Aggregated fractions of phases in the case of incomplete austenitization are assumed during cooling as a sum of fractions transformed from austenite and reminder untransformed structure η_k.

Temperatures and cooling rates in temperature range [800÷500]°C determine volumetric fractions of phases forming from austenite during cooling. For diffusive phase transformations such as bainite, pearlite or ferrite a fraction of a new phase growth is determined on the basis of JMA formula:

$$\begin{gathered} \eta_{(\cdot)}(T,t) = \eta_{(\cdot)}^{\%} \tilde{\eta}_A (1 - \exp(-b(t(T))^n)), \\ \underline{\eta}_A - \sum_{k=1}^{4} \eta_k \geq 0, \qquad \sum_{k=1}^{5} \eta_k^{\%} = 1, \end{gathered} \tag{3.4}$$

where $\eta_{(\cdot)}^{\%}$ is the maximal phase fraction for determined cooling rate estimated on the basis of CCT diagram, $\widetilde{\eta}_A$ is the austenite fraction formed due to heating, while η_k is a phase fraction formed before calculated phase transformation during cooling. Coefficients b and n are calculated using Eq. (3.2).

Volumetric fraction of martensite (ηM) is estimated using the Koistinen–Marburger (KM) formula:

$$\eta_M(T) = \eta_{(\cdot)}^{\%} \tilde{\eta}_A (1 - \exp(-k(M_s - T)^m)), \qquad T \in [M_s, M_f], \tag{3.5}$$

where coefficient $k = -\ln(1 - \eta_{\max})/(M_s - M_f)$ depends on martensite phase start and final temperatures (M_s and M_f).

The increase of isotropic strain generated by the temperature field and phase transformations in the solid state in heating and cooling processes is determined according to the following formula:

$$d\varepsilon^{TPh} = \sum_i \alpha_i \eta_i dT - \operatorname{sgn}(dT) \sum_i \varepsilon_i^{Ph} d\eta_i, \tag{3.6}$$

where $i = \mathrm{A, F, P, B, M}$ (austenite, bainite, ferrite, pearlite, martensite and pearlite), $\alpha_i = \alpha_i(T)$ is thermal expansion coefficient for each phase, $\varepsilon_i^{Ph} =$

$\varepsilon_i^{ph}(T)$ is an isotropic structural strain resulting from the transformation of the base structure into austenite during heating and each phase arising from austenite during cooling, $d\eta_i$ is a volumetric fractions of phases, $\mathrm{sgn}(\cdot)$ is a sign function.

In order to determine the thermal expansion coefficients and structural strains of each structure constituent the dilatometric analysis is performed. Obtained dilatometric curves are compared to simulated thermal and structural strain. Estimated values are presented in Table 3. The comparison between exemplary simulated curves and experimental results are illustrated in Fig. 4 with corresponding kinetics of phase transformations.

Table 3. Thermal expansion coefficients and structural strains of structure constituents.

Constituent	Thermal expansion coefficient $\alpha_i \times 10^{-6}(1/K)$		Structural strain $\varepsilon_i^{ph} \times 10^{-3}$	
Austenite	α_A	21.0	ε_A	3.5
Ferrite	α_F	14.7	ε_F	3.0
pearlite	α_P	13.7	ε_P	4.0
Bainite	α_B	12.5	ε_B	3.5
Martensite	α_M	12.0	ε_M	5.7

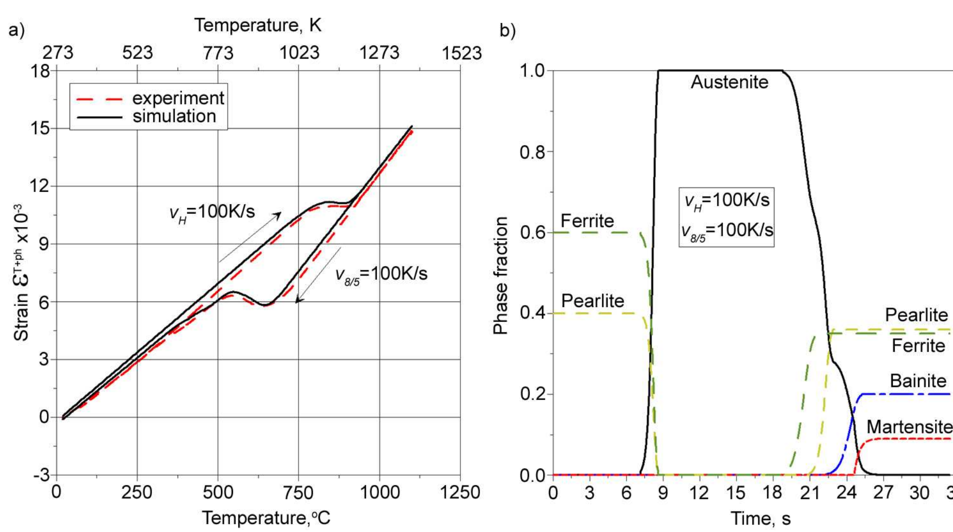

Fig. 4. Experimentally obtained and calculated a) isotropic strain and b) corresponding kinetics of phase transformations. Cooling rate $v_{8/5} = 200$ K/s.

4. Numerical modelling

Governing differential equations describing thermal phenomena in the process are numerically solved using Chorin's projection method with finite volume method (FVM) [24] to estimate the velocity field of the liquid metal in the fusion zone as well as finite element method (FEM) [25] to estimate the temperature field in the laser heated material. Analyzed domain is discretized by cubic elements used as control volumes in FVM and finite linear elements in FEM. Velocity components are calculated at nodal points, placed in the middle of each control volume face in FVM, while the pressure and density are calculated at the centre of control volumes (in FVM the so-called staggered grid is used to avoid odd-even decoupling between the pressure and velocity).

Numerical solutions are implemented into computer solver written in Object Pascal. Developed computational model assumes that fluid flow in the fusion zone is laminar and liquid steel is the incompressible viscous fluid. Designed numerical algorithm is presented in Fig. 5.

The projection method is used in the first module of the algorithm. This method assumes the estimation of liquid material velocity field in two steps [24]. In the first step Eq. (2.2) is solved without momentum changes due to pressure forces, according to the following formula:

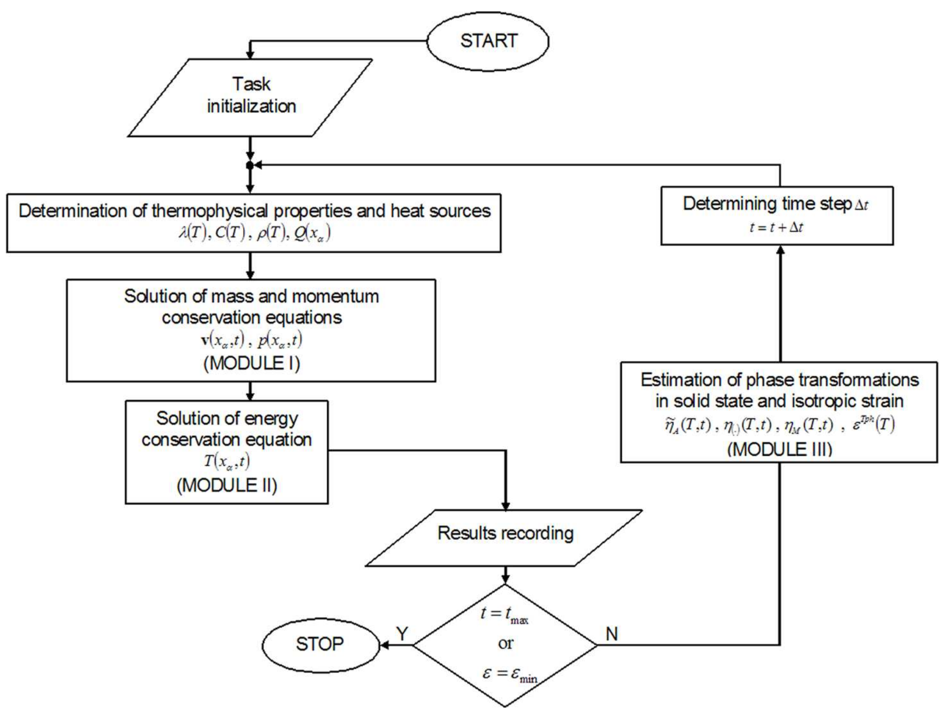

FIG. 5. Solution algorithm.

$$\frac{\mathbf{v}^{s+1}-\mathbf{v}^s}{\Delta t^s} = -\mathbf{A}^s + \frac{1}{\rho^s}(\mathbf{D}^s + \mathbf{S}^s - \nabla p) + \mathbf{f}^s, \tag{4.1}$$

where $\mathbf{A}^s$ is the advective term, $\mathbf{D}^s$ is viscosity (diffusive) term, $\mathbf{S}^s$ stands for fluid flow through porous medium, $\mathbf{f}^s$ is the mass force corresponding to natural convection of liquid metal. In order to calculate terms in Eq. (4.1) central difference quotients are used for each control volume in staggered grid.

The temporary velocity $\mathbf{v}^*$ is projected onto $\mathbf{v}^{s+1}$ in the second step, according to the following formula:

$$\frac{\mathbf{v}^{s+1}-\mathbf{v}^*}{\Delta t} = -\frac{1}{\rho^s}(\nabla p^{s+1}). \tag{4.2}$$

Assuming fulfilment of the continuity equation $\nabla \cdot \mathbf{v}^{s+1} = 0$ the pressure can be calculated at every simulation time from the solution of the following Poisson's equation:

$$\nabla \cdot \left(\frac{1}{\rho^s}(\nabla p^{s+1})\right) = \frac{1}{\Delta t}\nabla \cdot \mathbf{v}^*. \tag{4.3}$$

The energy conservation equation is solved in FEM in the second module of solution algorithm using method of weighted residuals in Petrov–Galerkin's formulation [25]. The weak form of equation (2.3) is expressed as follows:

$$\int\limits_{\Omega} \varphi[\nabla \cdot (\lambda \nabla T) + \tilde{Q}]\, d\Omega = \int\limits_{\Omega} \varphi C_{ef} \dot{T} d\Omega, \tag{4.4}$$

where $\varphi = \varphi(x_\alpha)$ is spatial weight function in Petrov–Galerkin's formulation.

Time integration of Eq. (4.4) leads to the following form:

$$\begin{aligned}\sum_e (K_{ij}^e + V_{ij}^e) \int\limits_t \vartheta(t) T_j(t) dt + \sum_e M_{ij}^e \int\limits_t \vartheta(t) \frac{\partial T_j(t)}{\partial t} dt \\ = \sum_e S_{ij}^e \int\limits_t \vartheta(t) Q_j^e(t) dt - \sum_{e^\Gamma} S_{ij}^\Gamma \int\limits_t \vartheta(t) \tilde{q}_j^e(t) dt,\end{aligned} \tag{4.5}$$

where $\vartheta(t)$ is a time weight function, K_{ij}^e is a local thermal conductivity matrix, V_{ij}^e is a local convection matrix, M_{ij}^e is a local heat capacity matrix, S_{ij}^e is a local coefficients matrix, Q_j^e is a local vector of internal sources efficiency, $\tilde{q}_j^e$ is a local vector of boundary fluxes, e is a finite element number, i and j are nodes numbers.

The final system of equations after time integration, is expressed as follows:

$$\begin{aligned}(\beta K_{ij} + M_{ij}) T_j^{s+1} \\ = [M_{ij} - (1-\beta) K_{ij}] T_j^s + \beta Q_i^{s+1} + (1-\beta) Q_i^s - \beta q_i^{*s+1} - (1-\beta) q_i^{*s},\end{aligned} \tag{4.6}$$

where β is a factor of integration over the time.

Developed algorithms require the verification in order to evaluate the accuracy of calculations. Therefore, benchmarking is performed on the basis of data presented in [26, 27] for the modelling of natural convection as well as the lid-driven cavity. Algorithm for the analysis of temperature field in Eq. (4.6) is compared with analytical solutions presented in [17] without the convective motion of the liquid material taken into account.

5. Results and discussion

Computer simulations of a single laser beam welding are performed without additional material for thin sheets made of S355 steel. Dimensions of analyzed plates are set to 150 × 30 × 4 mm. On the basis of performed calculations the geometry of fusion zone and heat affected zone is estimated as well as structural composition and isotropic strain of welded joints for assumed different welding speeds.

Table 4. Thermophysical properties assumed in computer simulations.

Nomenclature	Symbol	Value
Solidus temperature	T_S	1750
Liquidus temperature	T_L	1800
Boiling point	T_b	3010
Ambient temperature	T_0	293
Specific heat of solid phase	c_S	650
Specific heat of liquid phase	c_L	840
Density of solid phase	ρ_S	7800
Density of liquid phase	ρ_L	6800
Latent heat of fusion	H_L	$270\ 10^3$
Latent heat of evaporation	H_b	76×10^5
Latent heat of phase transformations in solid state	$\mathrm{H}_{A\to F}$, $\mathrm{H}_{A\to P}$ $\mathrm{H}_{A\to B} = \mathrm{H}_{A\to M}$	$8{\times}10^4$, $9{\times}10^4$, $11.5{\times}10^4$
Thermal conductivity of solid phase	λ_S	45
Thermal conductivity of liquid phase	λ_L	35
Gravitational acceleration	$\mathbf{g}$	9,81
Convective heat transfer coefficient	α_k	50
Boltzmann's constant	σ	5.67×10^{-8}
Thermal expansion coefficient	β_T	4.95×10^{-5}
Surface radiation emissivity	ε	0.5
Dynamic viscosity	μ	0.006
Average solid particle diameter	d_0	0.0001

Analyzed domain is discretized with different spatial step. Approximation of spatial step is linear, changing from 0.05 mm in the centre of laser beam heat source up to 0.5 mm outside the heat affected zone. In lower temperatures rarer spatial step is assumed, linearly approximated from 0.5 mm up to 2 mm. Thermophysical properties of S355 steel assumed in calculations are summarized in Table 4.

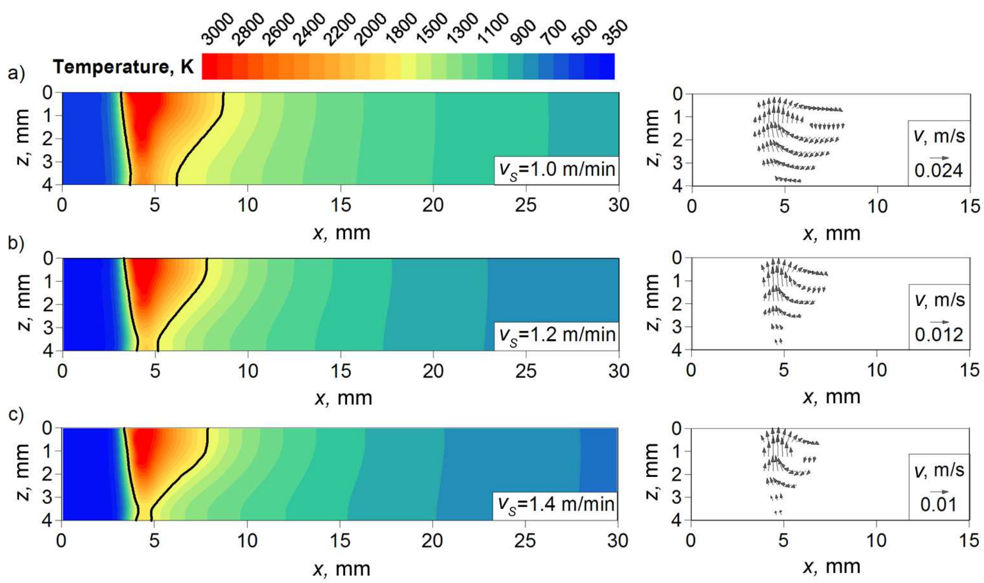

Fig. 6. Temperature field and melted material velocity field in the longitudinal section of the joint for three different welding speeds.

Technological parameters used in simulations are assumed on the basis of literature research [13, 18] and own research [17]. Laser beam power distribution is described by CIN model Eq. (2.11) with assumed heat source power $Q_L = 3.2$ kW, beam radius $r_0 = 1$ mm, laser beam efficiency $\eta_L = 85\%$ and the depth of penetration $s = 5$ mm. Different welding speeds $v_s = 1.0$, $v_s = 1.2$ and $v_s = 1.4$ m/min are assumed in computer simulations in order to analyze the influence of chosen process parameters on the geometry of the weld and structure composition of the joint.

Temperature field (on the left side) and melted material velocity field (on the right side) are presented in the longitudinal section (Fig. 6) in the middle of heat source activity zone ($y = 0$) and in the cross-section (Fig. 7) for three different welding speeds. Solid line points out the melted zone boundary, whereas dashed line marks the boundary of HAZ ($T_g \approx 1000$ K). It can be noticed that for low welding speed ($v_s = 1.0$ m/min) the fusion zone is wider and molten steel velocity is higher (Fig. 6). Calculated temperature field in the cross-section of the joint

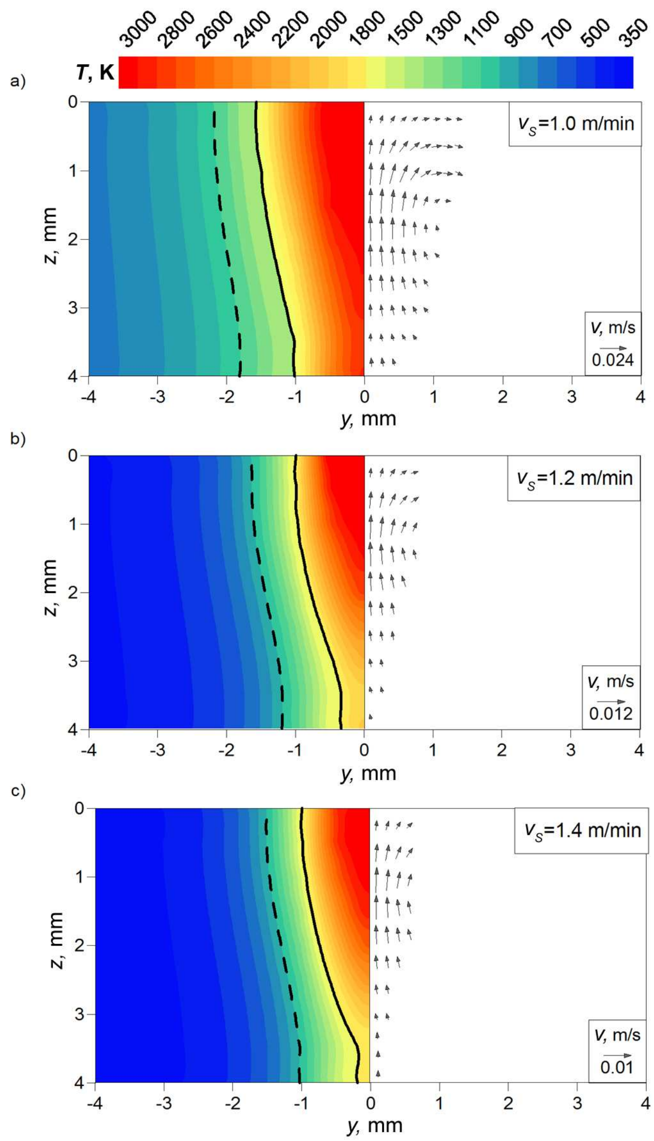

Fig. 7. Temperature field and melted material velocity field in the cross -section of the joint for three different welding speeds.

(Fig. 7) allows for the determination of weld and HAZ geometry. It is observed that motion of melted material in the welding pool has significant influence on the weld shape, especially at lower welding speed. Maximum velocity of melted steel is reached in the middle of heat source activity zone. Also at lower welding speed much wider HAZ is observed (Fig. 7a).

Figures 8 and 9 present comparison of thermal cycles for three welding speeds for chosen points at the top surface of the joint. In these figures, solidus, liquidus and boiling temperatures are marked as well as temperature range [800°C; 500°C] where cooling rates are determined for the analysis of phase transformations in the solid state. It can be observed that maximum temperatures exceeds the boiling point of steel (T_b), leading to the evaporation and creation of the keyhole. After the solidification, the workpiece is rapidly cooled to the ambient tempera-

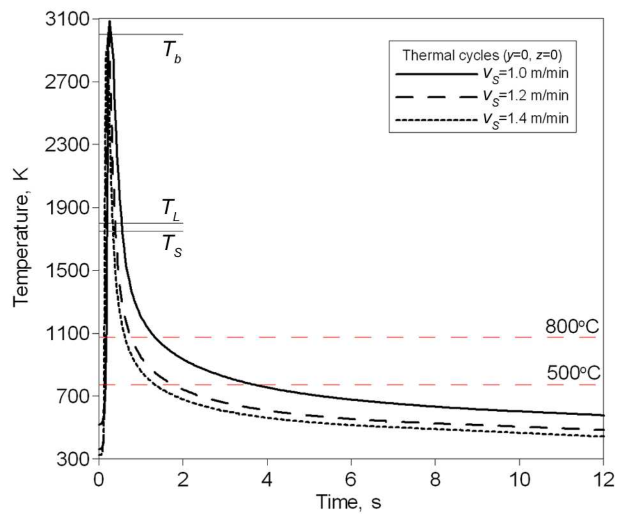

Fig. 8. Thermal cycles at a chosen point (y=0, z=0) for three different welding speeds.

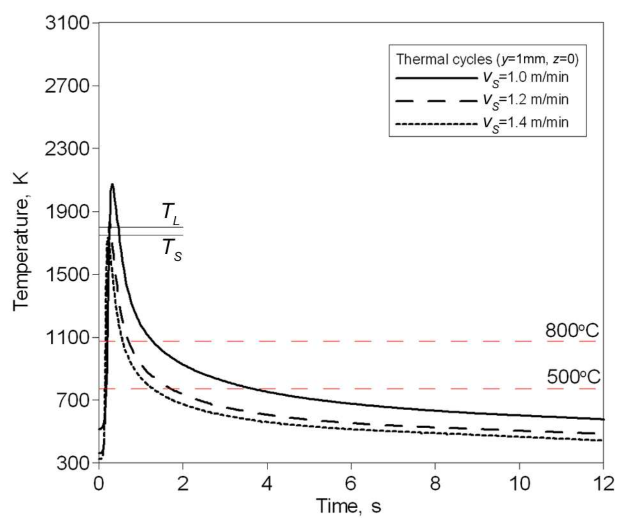

Fig. 9. Thermal cycles at a chosen point ($y = 1$ mm, $z = 0$) for three different welding speeds.

ture. It can be noticed that increasing welding speed contributes to the increase of cooling rates.

The kinetics of phase transformations in the solid state and isotropic strain are calculated on the basis of obtained thermal cycles. Figure 10 presents thermal

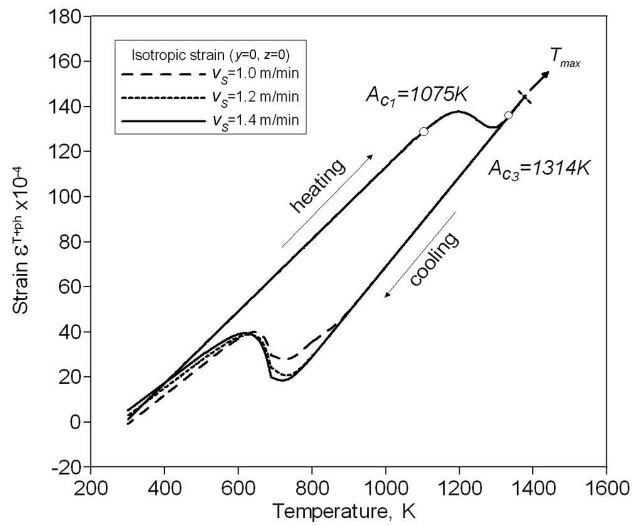

FIG. 10. Thermal and structural strain for three different welding speeds, at a chosen point ($y = 0$, $z = 0$) of the joint.

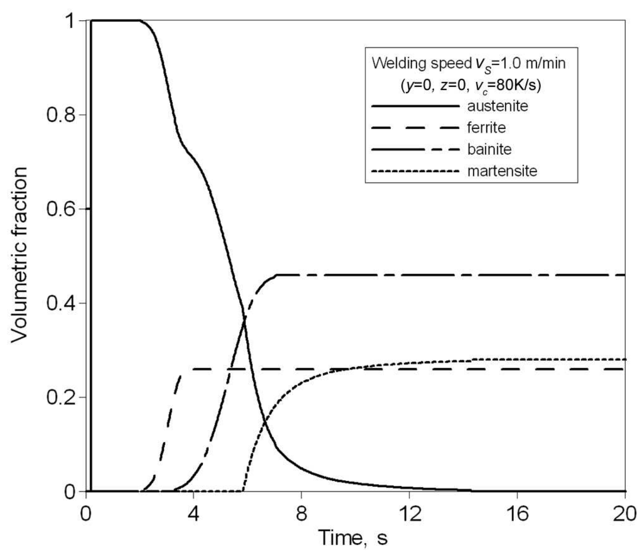

FIG. 11. Kinetics of phase transformations in solid state for welding speed $v_s = 1.0$ m/min, at a chosen point ($y = 0$, $z = 0$).

and structural strains in the material point ($y = 0$, $z = 0$). Various isotropic deformations are observed in this point during cooling, depending on estimated cooling rates.

Figures 11–13 present the kinetics of phase transformations at a chosen thermal cycle ($y = 0$, $z = 0$) for three different welding speeds, corresponding to

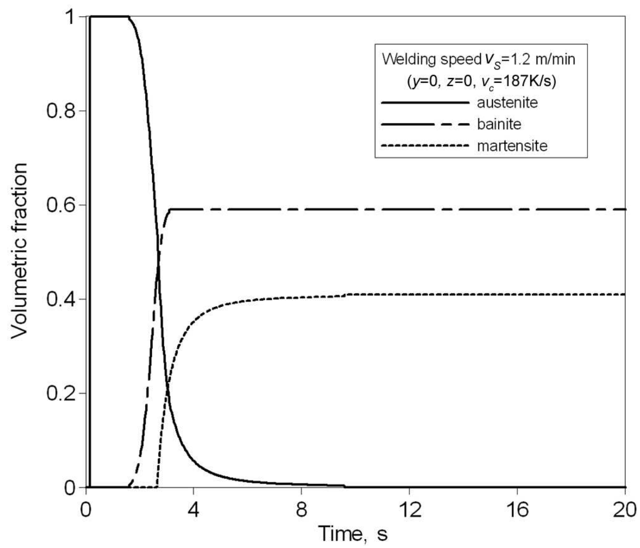

FIG. 12. Kinetics of phase transformations in solid state for welding speed $v_s = 1.2$ m/min, at a chosen point ($y = 0$, $z = 0$).

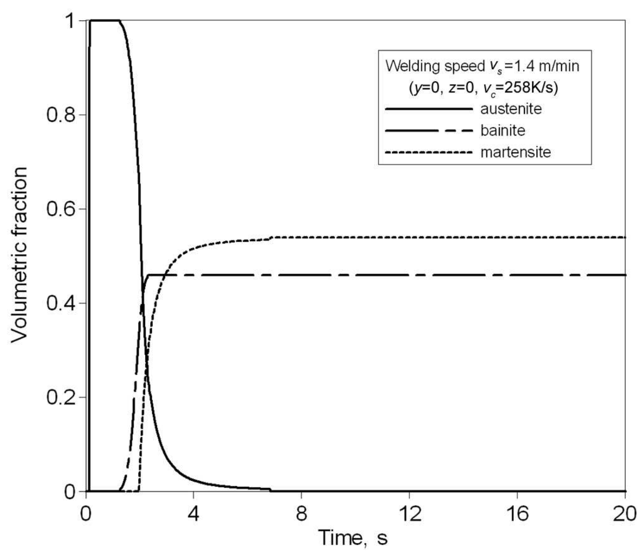

FIG. 13. Kinetics of phase transformations in solid state for welding speed $v_s = 1.4$ m/min, at a chosen point ($y = 0$, $z = 0$).

isotropic strain illustrated in Fig. 10. It can be noticed that increasing cooling rates determine the volumetric fraction of martensite in the joint and in consequence the level of joint hardening.

The prediction of structure composition is performed for each thermal cycle in the weld and HAZ on the basis of numerically estimated kinetics of phase transformations in the solid state. Volumetric fractions of ferrite+pearlite (F+P),

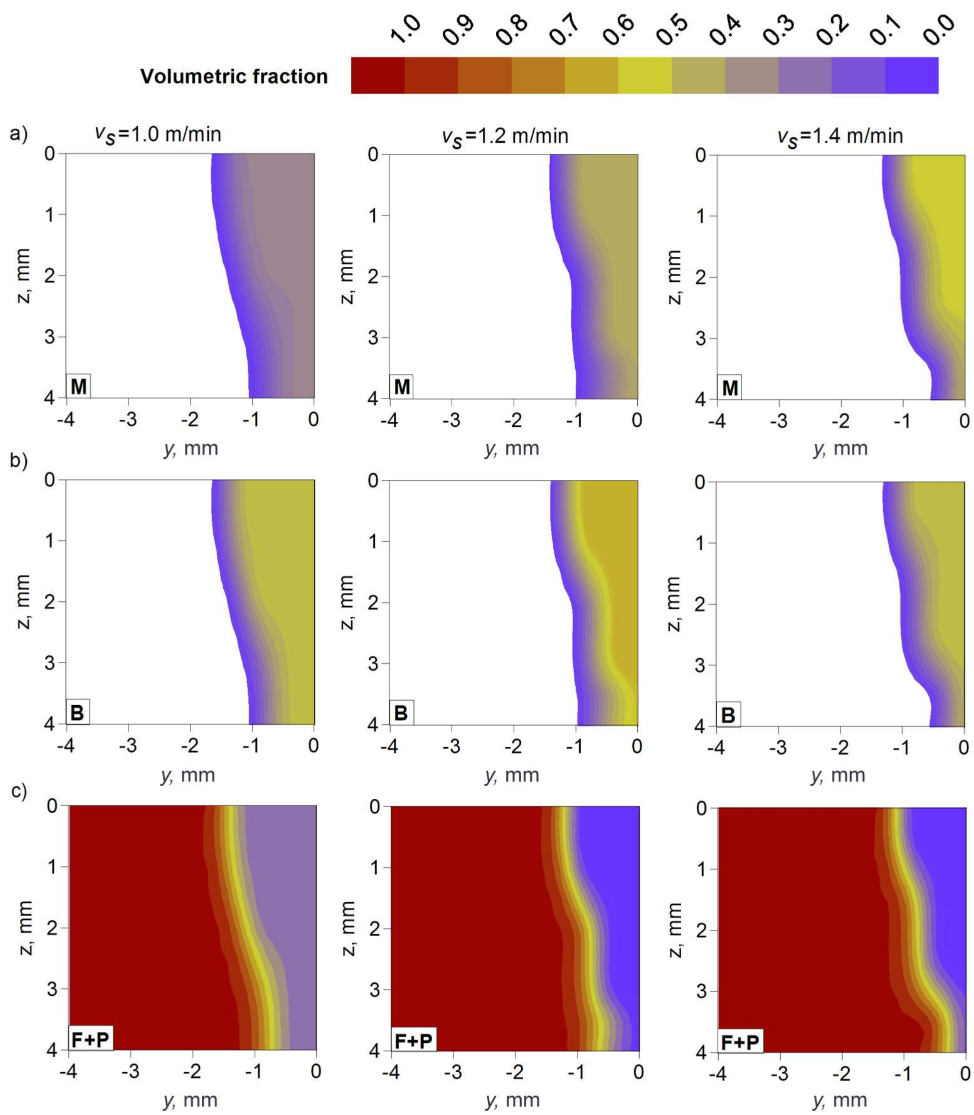

Fig. 14. The distribution of final fractions of structure constituents in the cross-section of the joint for three different welding speeds.

bainite (B) and martensite (M) in the cross-section of the joint are presented in Fig. 14 for three chosen welding speeds. As shown in this figure, for the first case ($v_s = 1.0$ m/min) final structure of the joint consists of ferrite, bainite and up to 30% martensite. Predicted martensite fraction increases with increasing welding speed up to 55% for $v_s = 1.4$ m/min because of the higher cooling rates occurring in the process.

6. Conclusions

Three-dimensional numerical model is developed for the numerical analysis of thermal phenomena and phase transformations in the solid state accompanying laser heating of thin sheets made of S355 steel. Temperature field and velocity field of melted metal in the fusion zone are obtained by the numerical solution into mass, momentum and energy conservation equations. Numerical solutions are implemented into self-made computer solvers allowing the prediction of the geometry of the fusion zone and HAZ as well as the structure composition of the joint and isotropic strain generated by the temperature field and phase transformations in the solid state. Computer simulations are performed for three different welding speeds in order to analyze the influence of chosen process parameters on the quality of welded joint. The following conclusions can be made from this study:

1. Laser welded joint is characterized by a narrow weld and HAZ. High cooling rates result in increasing hardening structures (martensite) in the thermal influence zone.
2. Significant differences in cooling rates are observed for chosen welding speeds contributing to the increase of martensite fraction in the weld and HAZ. There is a significant increase in cooling rates for $v_s = 1.4$ m/min where martensite fraction is up to 55%.
3. Changes in cooling rates resulted in various start and final temperatures and times of each occurring phase transformation, consequently changing isotropic strain arising during cooling of laser welded joints.
4. Presented numerical analysis provides a starting point for the modelling of thermomechanical states in laser processing.
5. Developed comprehensive computational model allows assessing the quality of the joint in terms of different process parameters and may be useful in industrial practice.

References

1. W.M. Steen, *Laser Material Processing*, Springer, London, 1991.
2. C. Dawes, *Laser Welding*, Abington Publishing, New York, 1992.

3. J. Pilarczyk, M. Banasik, J. Dworak, S. Stano, *Technological applications of laser beam welding and cutting at the Instytut Spawalnictwa*, Przegląd Spawalnictwa, **5-6**, 6–10, 2006 [in Polish].

4. X. Jin, L. Li, Y. Zhang, *A study of fresnel absorption and reflections in the keyhole in deep penetration laser welding,* Journal of Physics D: Applied Physics, **35**, 2304–2310, 2002.

5. L. Han, F.W. Liou, *Numerical investigation of the influence of laser beam mode on melt pool*, International Journal of Heat and Mass Transfer, **47**, 4385–4402, 2004.

6. T. Mościcki, J. Hoffman, Z. Szymański, *Modelling of plasma formation during nanosecond laser ablation*, Archives of Mechanics, **63**, 2, 99–116, 2011.

7. A. De, T. DebRoy, *Reliable calculations of heat and fluid flow during conduction mode laser welding through optimization of uncertain parameters*, Welding Journal, **84**, 101–112, 2005.

8. M.J. Torkamany, J. Sabbaghzadeh, M.J. Hamedi, *Effect of laser welding mode on the microstructure and mechanical performance of dissimilar laser spot welds between low carbon and austenitic stainless steels*, Materials & Design, **34**, 666–672, 2012.

9. W. Piekarska, M. Kubiak, *Theoretical investigations into heat transfer in laser-welded steel sheets*, Journal of Thermal Analysis and Calorimetry, **110**, 159–166, 2012.

10. S.A. Tsirkas, P. Papanikos, T.H. Kermanidis, *Numerical simulation of the laser welding process in butt-joint specimens*, Journal of Materials Processing Technology, **134**, 59–69, 2003.

11. R. Rai, S.M. Kelly, R.P. Martukanitz, T.A. Debroy, *Convective heat-transfer model for partial and full penetration keyhole mode laser welding of a structural steel*, Metallurgical and Materials Transactions A, **39A**, 98–112, 2008.

12. E. Ranatowski, *Thermal modelling of laser welding. Part I: The physical basis of laser welding*, Advances in Materials Science, **1**, 34–40, 2003.

13. F. Lu, X. Tang, H. Yu, S. Yao, *Numerical simulation on interaction between TIG welding arc and weld pool,* Computational Materials Science, **35**, 458–465, 2006.

14. S. Serajzadeh, *Modelling of temperature history and phase transformations during cooling of steel*, Journal of Materials Processing Technology, **146**, 311–317, 2004.

15. W.S. Chang, S.J. Na, *A study on the prediction of the laser weld shape with varying heat source equations and the thermal distortion of a small structure in micro-joining*, Journal of Materials Processing Technology, **120**, 208–214, 2002.

16. K. Abderrazak, S. Bannour, H. Mhiri, G. Lepalec, M. Autric, *Numerical and experimental study of molten pool formation during continuous laser welding of AZ91 magnesium alloy*, Computer Materials Science, **44**, 858–866, 2009.

17. W. Piekarska, *Numerical analysis of thermomechanical phenomena during laser welding process. Temperature field, phase transformations and stresses*, Seria Monografie 135, Wydawnictwo Politechniki Częstochowskiej, Częstochowa, 2007 [in Polish].

18. K. Mundra, T. DebRoy, *Calculation of weld metal composition change in high-power conduction mode carbon dioxide laser-welded stainless steel,* Metallurgical Transactions B, **24B**, 2, 145–155, 1993.

19. K.J. Lee, *Characteristics of heat generation during transformation in carbon steels*, Scripta Materialia, **40**, 735–742, 1999.

20. D. Gery, H. Long, P. Maropoulos, *Effects of welding speed, energy input and heat source distribution on temperature variations in butt joint welding,* Journal of Materials Processing Technology, **167**, 393–401, 2005.

21. P. Lacki, K. Adamus, *Numerical simulation of the electron beam welding process*, Computers & Structures, **89**, 977–985, 2011.

22. P. Lacki, K. Adamus, K. Wojsyk, M. Zawadzki, Z. Nitkiewicz, *Modeling of heat source based on parameters of electron beam welding process,* Archives of Metallurgy and Materials, **56**, 2, 455–462, 2011.

23. W. Piekarska, M. Kubiak, A. Bokota, *Numerical simulation of thermal phenomena and phase transformations in laser-arc hybrid welded joints*, Archives of Metallurgy and Materials, **56**, 409–421, 2011.

24. S.V. Patankar, *Numerical Heat Transfer and Fluid Flow*, Taylor & Francis, USA, 1990.

25. O.C. Zienkiewicz, R.L. Taylor, *The finite element method*, 5th ed., Vol. 1–3, Butterworth-Heinemann, New York, 2000.

26. G. De Valh Davis, *Natural convection of air in a square cavity a bench mark numerical solution*, International Journal of Numerical Methods in Fluids, **3**, 249–264, 1983.

27. O. Botella, R. Peyret, *Benchmark spectral results on the lid-driven cavity flow*, Computers & Fluids, **27**, 421–433, 1998.

Received October 18, 2013; revised version August 26, 2014.